

On-Policy and Pixel-Level Grasping Across the Gap Between Simulation and Reality

Dexin Wang, Faliang Chang, Chunsheng Liu, *Member, IEEE*, Rurui Yang, Nanjun Li, and Hengqiang Huan

Abstract—Grasp detection in cluttered scenes is a very challenging task for robots. Generating synthetic grasping data is a popular way to train and test grasp methods, as is Dex-Net and GraspNet; yet, these methods sample training grasps on 3D synthetic object models, but evaluate at images or point clouds with different sample distributions, which reduces performance due to covariate shift and sparse grasp labels. To solve existing problems, we propose a novel on-policy grasp detection method, which can train and test on the approximate distribution with dense pixel-level grasp labels generated on RGB-D images. An Orthographic-Depth Grasp Generation (ODG-Generation) method is proposed to generate an orthographic depth image through a new imaging model of projecting points in orthographic; then this method generates multiple candidate grasps for each pixel and obtains robust positive grasps through flatness detection, force-closure metric and collision detection. Then, a large comprehensive Pixel-Level Grasp Pose Dataset (PLGP-Dataset) is constructed and released; distinguished with previous datasets with off-policy data and sparse grasp samples, this dataset is the first pixel-level grasp dataset, with the on-policy distribution. Lastly, we build and test a series of grasp detection networks with a data augmentation process for imbalance training, which learn grasp poses in a decoupled manner on the input RGB-D images. Extensive experiments show that our on-policy grasp method can largely overcome the gap between simulation and reality, and achieves the state-of-the-art performance. Code and data are provided at <https://github.com/liuchunsense/PLGP-Dataset>.

Index Terms—grasp detection, on-policy grasp, pixel-level grasp, orthographic depth image

I. INTRODUCTION

Object grasping is a core issue in the field of robots [1][2]. Recently, many algorithms have claimed to be effective for handling stacked scenarios as well as grasping novel objects. There are currently two problems that are still unresolved, including on-policy grasping strategy and pixel-level exhaustive grasping generation.

(1) Some approaches train and test grasp policy on two different sample distributions [3–8], and this process belongs to off-policy grasping strategy. Parts of these methods sample training grasps that are constrained to known 3D object surfaces while the learned policy samples grasps from observations, such as Dex-Net [3–5] and GraspNet [6]. Wang *et al.* [8] manually labelled grasps on the image, but humans cannot handle complex sample distributions. The difference in distribution makes the trained network unable to fit the test data, which may lead to reduced performance due to covariate shift [9].

All authors are with the School of Control Science and Engineering, Shandong University, Ji'nan, Shandong 250061, China (e-mail: flchang@sdu.edu.cn, liuchunseng@sdu.edu.cn). (Corresponding author: Faliang Chang, Chunsheng Liu)

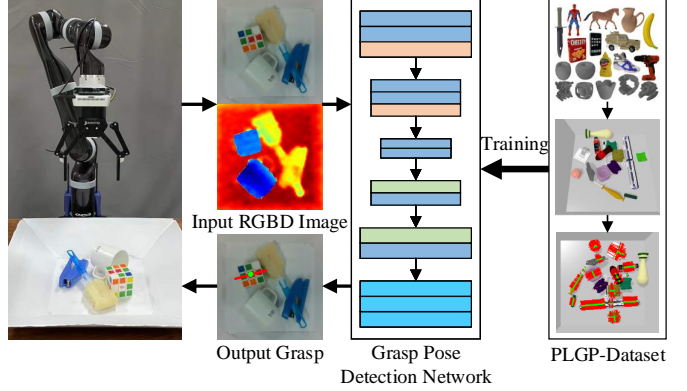


Fig. 1. Our on-policy grasping method. The grasp pose detection network is trained to generate grasp poses from RGB-D images using the PLGP-Dataset which consists of 45,550 synthetic RGB-D images and associated pixel-level grasp labels. Based on the output grasp with the maximal confidence, a robot is capable of successfully grasping objects.

(2) The training grasps of previous dataset are not exhaustive. Dex-Net [3] generate grasp labels by sampling on the 3D object models due to large computation consuming of traversing the voxels. Sparse labels cannot contain all positive samples and reduce sample variance, thereby reducing the generalization ability of the grasp policy.

For the first problem, we compute the quality of all grasp configurations in image space to obtain training grasps and validate the learned policy. Since the RGB-D images based on the pinhole model cannot capture the information of occluded positions, previous methods cannot compute grasp poses based on images. We generate orthographic depth images by projecting points in the scene orthographic to the imaging plane, and take each pixel as the grasp center to calculate the grasp quality and generate training grasps. This method makes the training and testing grasps of the network contain approximate distributions of positive and negative samples. In RL, on-policy methods use the learned policy to collect data and avoid disparity in the distribution of target policy (i.e., training) and current policy (i.e., testing) [10] [11]. Drawing inspiration from [9], we refer to this as the *on-policy* method and distinguish this from prior methods that train and test on two different distributions.

For the second problem, we compute multiple robust grasp poses for each pixel in the image. Since computing the grasp centered on each voxel is extremely time-consuming, previous methods use sampling instead of traversal. We traverse the pixels of the depth image to automatically generate dense pixel-level labels that covering the full grasp parameter space.

Based on the above solutions, we propose an Orthographic-Depth Grasp Generation (ODG-Generation) method. The method first renders the camera depth image and orthographic depth image for the cluttered scene in the PyBullet simulation environment [12] based on the pinhole model and the orthographic projection model, respectively. Then, multiple candidate grasp poses are generated for each pixel in the camera depth image. Finally, some checks based on orthographic depth image are used to screen out robust positive grasps. Based on the automatic ODG-Generation, we build the first Pixel-Level Grasp Pose Dataset (PLGP-Dataset) that can serve as a base for training and evaluating grasp detection algorithms. PLGP-Dataset contains 45,550 RGB-D images taken from the different viewpoints of cluttered scenes. Each image is densely annotated, bringing over 58 million grasp poses.

We further construct an end-to-end network for learning grasp poses. To verify that our network performs better, we replace the backbone module with five semantic segmentation networks and two grasp detection networks. A novel data augmentation method is proposed to increase positive samples to reduce the impact of data imbalance on network training. Meanwhile, we contribute a simulation bin-picking benchmark that can provide synthetic RGB-D images and point clouds embedded with noise, and drive the simulated robotic arm to grasp object according to a given grasp pose.

The proposed on-policy method is shown in Fig. 1. We design rich experiments to demonstrate that our on-policy method outperforms the off-policy methods, and the pixel-level grasp labels improve generalization. Besides, we compare our method with previous methods in the benchmark, and conduct robotic experiments in real-world. Experiments demonstrate that our method can overcome the gap between simulation and reality, and achieves the state-of-the-art performance.

The contributions of our study are summarized as follows:

- We propose an on-policy grasp method that avoid covariate shift caused by training and testing the network on different distributions.
- We propose an Orthographic-Depth Grasp Generation (ODG-Generation) method to collect RGB-D images and generate pixel-level grasp labels.
- The first Pixel-Level Grasp Pose Dataset (PLGP-Dataset) is built which can serve as a base for training and evaluating grasp pose detection algorithms.
- Based on the PLGP-Dataset, we train a grasp detection network which achieve the state-of-the-art performance.

II. RELATED WORK

The goal of grasp detection is to output a gripper pose using the visual information of cluttered scenarios, and the gripper can stably grasp the target when closing the jaws in this posture. The methods can be roughly divided into analytic methods and empirical methods [20]. Analytic methods first use the object model to generate stable grasps, and then obtain the reachable grasp according to the object pose in the scene. Yet, they are usually not applicable to objects

whose models are unknown. In contrast, empirical methods do not require object 3D models; they train the grasp model using known objects and use the model to detect the grasp posture of unknown objects [21][22][23]. In recent years, deep learning based methods have attracted the attention of many researchers.

Dataset. In order to train the grasp detection network, many datasets are proposed. Cornell dataset [13] collects RGB-D images of scenes containing a single object, and manually annotates rectangle grasp pose. [15][14] use real robots for random grasping, and records the successful grasps pose as labels. These dataset generation methods are time-consuming and insufficient to cover all the grasp parameter space. To avoid such problem, [16] uses 3D object models to build cluttered scenes in simulation environment, and uses simulation robots to collect grasp labels. The simulation-based method improves efficiency, but the grasp labels are still sparse. Mahler *et al.* first calculate 6-DOF grasps on the 3D object models through force-closure metric [24], then obtains the 4-DOF grasp pose perpendicular to the table [5][4]. To avoid the gap from simulation to reality, Fang *et al.* construct 3D models of real objects to sample 6-DOF grasp poses, and record point clouds of real stacked scenes to train grasp detection networks [6]. However, networks trained on these datasets need to fit functional relationships from images or point clouds to grasp poses generated based on 3D models, and the difference in data distribution reduces the performance of networks. On the contrary, we propose a label generation method that works directly on depth images and avoids differences in the data distribution of training network.

Network. Based on different grasp pose representations, grasp detection networks are mainly divided into three categories: grasp quality classification networks, 4-DOF networks based on RGB-D images, and 6-DOF networks based on point clouds. Based on grasp quality classification networks, Dex-Net [3–5] first samples multiple candidate grasp poses on the depth image, and then uses the network to evaluate the quality of each grasp. This method is less efficient and the candidate grasps cannot cover the grasp parameter space. Based on 4-DOF networks, discrete or pixel-level 4-DOF grasp poses are predicted end-to-end [8, 25–29]. Fewer degrees of freedom limit the reach of the gripper. Based on 6-DOF networks, sparse 6-DOF grasp poses are predicted in a decoupled manner [6][30–34]. However, the extreme imbalance of positive and negative samples makes the 6-DOF networks difficult to train. In this work, we validate that the 4-DOF network trained on our new dataset performs better than previous 6-DOF networks.

III. ORTHOGRAPHIC-DEPTH GRASP GENERATION METHOD

A. Overview

As far as the literature we can find, most previous grasp datasets are manually annotated or automatically annotated based on sampling. Due to the deviation between human subjectivity and actual grasping, the manually labeled grasp poses are inaccurate [13]. GraspNet [6] and Dex-Net [4] first

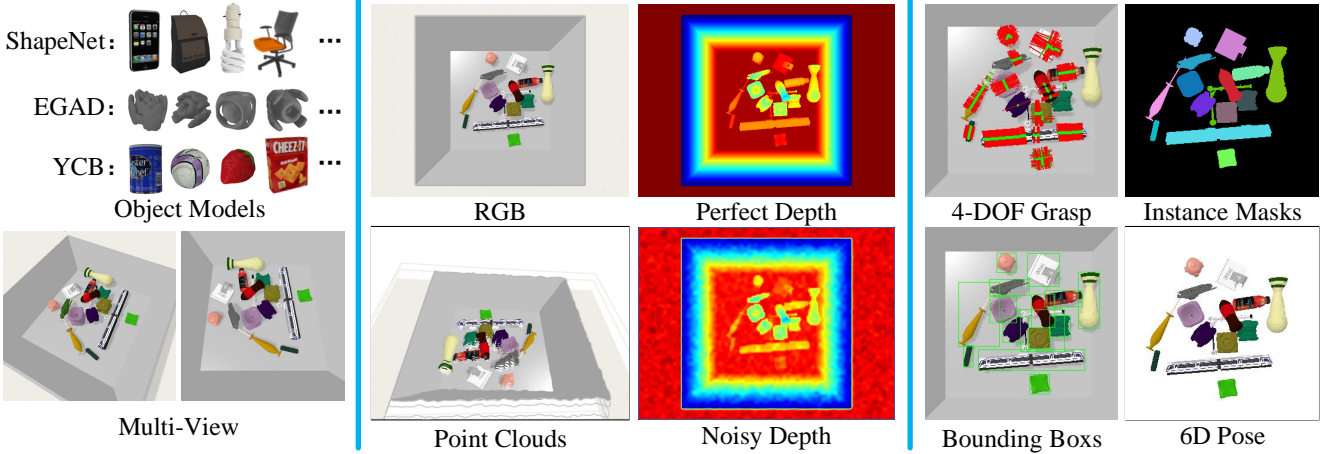


Fig. 2. The key components of PLGP-Dataset. RGB-D images are rendered in pybullet simulation environment from different views. The grasp poses, the 6D pose of each object, the bounding boxes and the instance masks are annotated.

TABLE I
SUMMARY OF THE PROPERTIES OF PUBLICLY AVAILABLE GRASP DATASETS.

Dataset	Grasps per image	Objects per image	Grasp label	Modality	Total objects	Total grasps	Total images	Data source	Automatized generation	Pixel level	On-policy
Cornell [13]	~8	1	Rect.	RGB-D	240	8,019	1,035	Cam.	No	No	No
Pinto <i>et al.</i> [14]	1	-	Rect.	RGB-D	150	50K	50K	Cam.	Yes	No	No
Levine <i>et al.</i> [15]	1	-	Rect.	RGB-D	-	800K	800K	Cam.	Yes	No	No
Dex-Net 2.0 [4]	1	1	4-DOF	Depth	1,500	6.7M	6.7M	Sim.	Yes	No	No
Dex-Net 2.1 [5]	1	~5	4-DOF	Depth	1,500	102.6K	102.6K	Sim.	Yes	No	No
Jacquard [16]	~20	1	Rect.	RGB-D	11k	1.1M	54K	Sim.	Yes	No	No
VMRD [17]	~20	~3	Rect.	RGB	-	100K	4,683	Cam.	No	No	No
Multi-Object [18]	~30	~4	Rect.	RGB-D	-	2904	96	Cam.	No	No	No
VR-Grasping-101 [19]	100	1	6-DOF	RGB-D	101	4.8M	10K	Sim.	Yes	No	No
GraspNet-1Billion [6]	3~9M	~10	6-DOF	RGB-D	88	1.2B	97K	Cam.	Half	No	No
PLGP-Dataset (Ours)	~1280	5/15	4-DOF	RGB-D	4,555	58M	45,550	Sim.	Yes	Yes	Yes

Rect.: Grasp rectangle [13]. Cam.: Camera. Sim.: Simulation.

sample grasp poses based on 3D object, and then screen out the grasp labels that do not collide with scene. However, sparse sampling cannot cover the full grasp space, which reduces the generalization of the network. To overcome these problems, we generate accurate and pixel-level grasp labels by traversing the pixels of the depth image.

Compared to previous dataset generation methods, our Orthographic-Depth Grasp Generation (ODG-Generation) method has three advantages: (1) Grasp labels are generated at the pixel level. We iterate over all pixels to compute grasps to avoid missing ground-truth. (2) The method is on-policy which enables grasp networks to train and test on the approximate distributions, while traditional methods train and test on different distributions. (3) The dataset construction process is automatic, so it can be easily and unlimitedly expanded.

Based on the ODG-Generation, we construct a dataset in cluttered scenario for pixel-level grasp pose detection named on PLGP-Dataset. The dataset contains 9,110 simulated cluttered scenes, and each contributes five RGB-D images from

different views, bringing 45,550 images in total. We also provide noise-added depth images to simulate real camera. The grasp poses for each image varies from 100 to 7,000, and in total our dataset contains over 58 million grasp poses. Besides, we also provide accurate object 6D pose annotations, object masks and bounding boxes. Fig. 2 illustrates the key components of our dataset. A summary of the properties of public grasp datasets can be found in Table I.

B. Data Collection

Our dataset contains 4,555 3D object models from three model datasets including: 2,204 synthetic models from ShapeNet [35], 70 laser scans from the YCB object database [36], and 2,281 synthetic models from EGAD [37]. All objects are diverse in shape and size, and scaled to fit the gripper. To collect data of cluttered scene, a simulated camera with a vertical field of view of 60 degrees and output image size of 480×640 is constructed. The camera intrinsic matrix is

calculated as follows:

$$M = \begin{bmatrix} \frac{240}{\tan(\text{fov}/2)} & 0 & 319.5 \\ 0 & \frac{240}{\tan(\text{fov}/2)} & 239.5 \\ 0 & 0 & 1 \end{bmatrix} \quad (1)$$

where fov is the vertical field of view.

Two sets of stacked scenes containing 5 and 15 random objects, respectively, are constructed. The objects are loaded into the simulation environment in random poses and fall freely into the tray to form cluttered scenes. For each scene, we collect 5 pairs of synchronized RGB-D images and corresponding camera poses from different viewpoints. Each camera pose T is calculated by initial pose T_i and offset pose T_o :

$$T = T_i \cdot T_o \quad (2)$$

where T_i denotes the pose that the camera is above the scene and the z-axis of camera is facing and perpendicular to the center of the tray. The translation vector t_o and euler angles R_o of T_o are defined by formula (3) and formula (4), respectively:

$$t_o = [2l\alpha_1 - l, 2l\alpha_2 - l, 0]^T \quad (3)$$

$$R_o = [-\tan(\frac{t_o[0]}{z}), \tan(\frac{t_o[1]}{z}), 0]^T \quad (4)$$

where l defines the maximum translation of the camera in the x-y plane, α_1 and α_2 are random numbers in the range $[0, 1]$ and specify the scale of camera translation along the x and y axes, respectively. z is the height of the camera from the tray when it is in the T_i pose. The pose T keeps the camera z-axis pointing at the center of the tray, so that all objects are included in the rendered image. The mask and pose of objects are exported by pybullet [12].

To stick as close as possible to real depth images, instead of only adding Gaussian noise to the perfect depth image as in [38], we follow the steps below to generate a more realistic depth image:

- (1) The values in the image are probabilistically set to 0, and the probability is calculated from the local gradient of the point. The processed image is:

$$I_1 = \begin{cases} 0, & \delta < f(\text{grad}) \\ I, & \text{otherwise} \end{cases} \quad (5)$$

where I denotes the perfect depth image, δ is a random number from 0 to 1, and $f(\text{grad})$ is a linear function that scales the gradients to the range $[0, 1]$. Points with large gradients have a high probability of being zeroed. The purpose is to simulate the missing regions of the depth image where the depth varies greatly.

- (2) Gaussian noise is added to the image I_1 to simulate the depth error of real cameras. The processed image is $I_2 = I_1 + \epsilon$ where ϵ is zero-mean Gaussian noise over pixel coordinates.
- (3) The image I_2 is sequentially scaled down by n times and upscaled to original size. The purpose is to remove small depth variations, which are often not captured by real RGB-D camera.

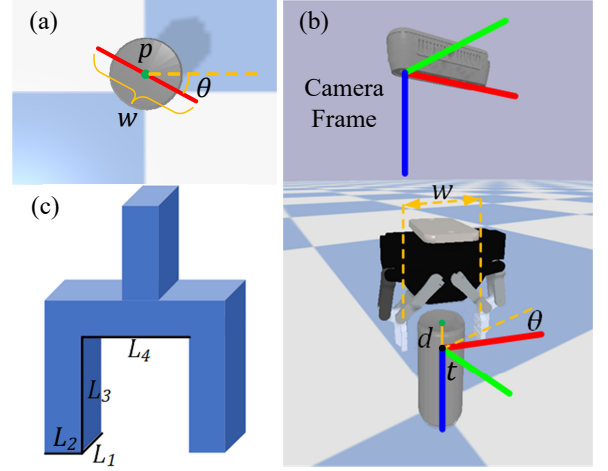


Fig. 3. (a) A 4-DOF grasp pose is defined by grasp point p , gripper approaching distance d , rotation around the camera z-axis θ and gripper width w . (b) The 6-DOF grasp pose calculated based on 4-DOF grasp pose. (c) Gripper size is denoted by $[L_1, L_2, L_3, L_4]$.

C. Grasp Definition

A 6-DOF grasp pose of parallel-jaw gripper is defined as:

$$g = [t, R, w] \quad (6)$$

where $t \in \mathbb{R}^{3 \times 1}$ denotes the center of the gripper, $R \in \mathbb{R}^{3 \times 3}$ denotes the gripper orientation and $w \in \mathbb{R}$ denotes the gripper opening width. For neural network that take images as input, directly learning the translation vector in $\mathbb{R}^{3 \times 1}$ and rotation matrix in $\mathbb{R}^{3 \times 3}$ is not intuitive [6]. Instead, we simplify the grasp pose g to a 4-DOF grasp \tilde{g} parallel to the camera's z-axis:

$$\tilde{g} = [p, d, \theta, w] \quad (7)$$

where $p \in \mathbb{R}^{2 \times 1}$ is the grasp point in the image, $d \in \mathbb{R}$ denotes the gripper approaching distance at p , and $\theta \in \mathbb{R}$ denotes the angle between the gripper closing direction and the image horizontal axis. The grasp pose g in camera coordinate system is calculated given \tilde{g} and camera intrinsic matrix M :

$$t = \frac{M^{-1}}{I(p)} \begin{bmatrix} p \\ 1 \end{bmatrix} + \begin{bmatrix} 0 \\ 0 \\ d \end{bmatrix} \quad (8)$$

$$R = \begin{bmatrix} \cos\theta & \sin\theta & 0 \\ -\sin\theta & \cos\theta & 0 \\ 0 & 0 & 1 \end{bmatrix} \quad (9)$$

where $I(p)$ denotes the value of the depth image I at grasp point p . Fig. 3 explains our formulation of grasp pose.

D. Orthographic Depth Image based Grasp Annotation

Most previous grasp datasets have sparse labels, and different distributions for training and testing, which reduces the performance. We compute dense grasp labels based on depth images. The usual depth image is generated based on TOF or structured light [39] which are actually pinhole imaging

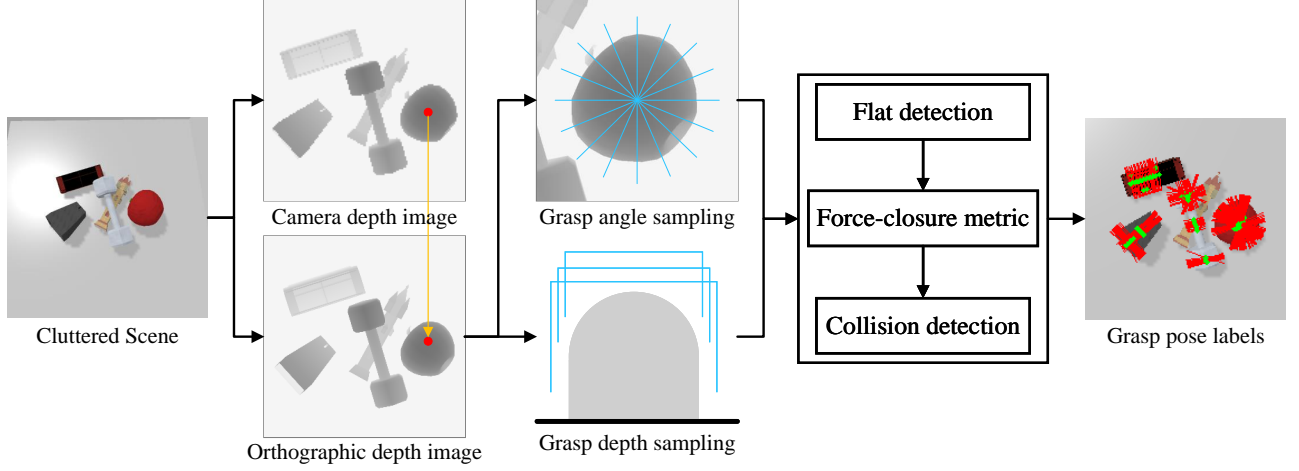


Fig. 4. Grasp pose annotation pipeline. The camera depth image and orthographic depth image are firstly rendered. Then the grasp angle and grasp depth are sampled for every point in camera depth image. The grasp width is calculated based on collision detection. Finally, a series of checks are performed to avoid invalid grasps. In the grasp pose labels, each green point represents grasp point p , and the direction and width of the red line centered on the green point represent the grasp angle θ and grasp width w , respectively.

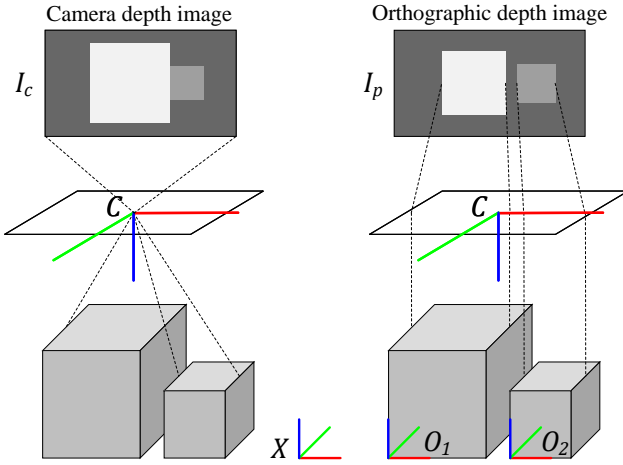


Fig. 5. The illustration of camera depth image I_c and orthographic depth image I_p . I_c is generated based on the pinhole imaging models. I_p is generated by scaling the x and y coordinates of point in the camera coordinate system C . The gap between two objects is lost in image I_c , and preserved in image I_p . The coordinate system of the scene consists of the simulated environment X , objects O and camera C .

models, so some information in the scene cannot be collected due to occlusion (Fig. 5 (a)). To solve the above problems, we propose an Orthographic-Depth Grasp Generation (ODG-Generation) method. The method first generates an orthographic depth image of the scene, then aligns the pixels in the image with the points in the camera depth image, and finally computes robust grasp poses using the orthographic depth image. The automated annotation pipeline is illustrated in Fig. 4, and the detailed process is described as follows.

For the convenience of description, let I_c and I_p denote the usual camera depth image and orthographic depth image, respectively, let O , X and C denote the coordinate system of the 3D object model, the simulation environment and the simulated camera respectively.

1) *Orthographic depth image generation:* Different from the camera depth image I_c , projection lines of points in the scene that generate orthographic depth image are parallel to each other instead of meeting at the optical center, which is illustrated in Fig. 5. In our experiments, the imaging plane of the image I_p coincides with the x - y plane of the camera coordinate system C , so the image I_p can be generated using the parameters of the simulated camera.

For a point p_O on the 3D object surface, the projected point $p_C = [x_C, y_C, z_C]$ in the camera coordinate system C is formulated as:

$$p_C = T_C^X \cdot T_X^O \cdot p_O \quad (10)$$

where $T_C^X \in \mathbb{R}^{4 \times 4}$ denotes the transformation matrix of coordinate system X relative to C , and $T_X^O \in \mathbb{R}^{4 \times 4}$ denotes the transformation matrix of coordinate system O relative to X . Then, the projected point $\tilde{p} = [\tilde{c}, \tilde{r}]^T$ of p_C in the image I_p of size $H \times W$ is formulated as:

$$\begin{bmatrix} \tilde{c} \\ \tilde{r} \\ 1 \end{bmatrix} = \begin{bmatrix} \eta & 0 & (W-1)/2 \\ 0 & \eta & (H-1)/2 \\ 0 & 0 & 1 \end{bmatrix} \cdot \begin{bmatrix} x_C \\ y_C \\ 1 \end{bmatrix} \quad (11)$$

where \tilde{c} and \tilde{r} respectively represent the column and row coordinates of \tilde{p} with the upper left corner of the image I_p as the origin. η is the projection ratio of the actual length in the image (5,000 in this study). The depth value of the image I_p at coordinate \tilde{p} is z_C . Fig. 5 shows the simplified principle of generating camera depth image and orthographic depth image, the gap between two objects is lost in image I_c , and preserved in image I_p .

2) *Pixel alignment:* In order to calculate the pixel-level grasp pose, we traverse each pixel on I_c and calculate the aligned point on the image I_p , and use the aligned point as the grasp center to calculate the robust grasp pose.

For a point p in the object mask in the camera depth image I_c , the projected point p_C in the camera coordinate system C is formulated as:

$$p_C = \frac{M^{-1}}{I_c(p)} \begin{bmatrix} p \\ 1 \end{bmatrix} \quad (12)$$

Then, the aligned point $\tilde{p} = [\tilde{c}, \tilde{r}]^T$ in the image I_p is calculated by:

$$\begin{bmatrix} \tilde{p} \\ 1 \end{bmatrix} = \begin{bmatrix} \eta & 0 & (W-1)/2 \\ 0 & \eta & (H-1)/2 \\ 0 & 0 & 1 \end{bmatrix} \cdot \begin{bmatrix} x_C \\ y_C \\ 1 \end{bmatrix} \quad (13)$$

3) *Grasp pose calculation*: We use the point \tilde{p} as the grasp center to calculate the robust grasp pose on the image I_p . For the point \tilde{p} , grasp angle θ and grasp depth d are searched in a two dimensional grid $\Theta \times D$, where $\Theta = \{\frac{k \cdot \pi}{K} | 0 \leq k < K, k \in N\}$ and $D = \{k \cdot g | 0 \leq k \cdot g < L_3, k \in N\}$. K is the number of grasp angle samples, we experimentally set $K = 18$. g is the grasp depth sampling interval, we set $g = 0.002 \text{ m}$. L_3 represents the maximum grasp depth of the gripper. Gripper width w is set to the opening width when the gripper just collides with the object plus tolerance (0.005 m in our experiments). In order to facilitate the calculation of the physical collision between the gripper and object, gripper size is denoted by $[L_1, L_2, L_3, L_4]$, as shown in Fig. 3(c). After these steps, we generate densely candidate grasp poses.

Then, a series of checks are performed to get positive grasps.

Flatness detection. Let Ω denote the points on the contact area between the gripper and the object in T_p . Flatness detection first fits the plane equation P of the point set Ω , and then calculates the variance Var of Ω with mean as the plane equation:

$$Var = \sum_{i=0}^{n-1} \frac{\Omega_i - P}{n} \quad (14)$$

where n is the number of points in the set Ω . The grasps with variance greater than threshold are filtered out.

Force-closure metric. Force-closure metric [24] is met if the grasp axis lie within the friction cone at contact point, so that the object will not slide relative to the gripper. The friction cone is defined by the halfangle $\alpha = \arctan(\mu)$, where μ is the coefficient of friction [40]. μ is set to 0.2 to ensure that most objects can be grasped stably.

Collision detection. Collision detection is performed to prevent the gripper from colliding with objects.

After these steps we can generate densely training grasps. Exhaustive computations approximate the distribution of training grasps to the distribution of learned policy testing, which avoids covariate shift and improves calculation efficiency. We conduct ablation experiments in Sec. V-B and Sec. V-C, and verify the significance of on-policy and pixel-level grasps. Besides, we conduct real world grasp experiment in Sec. V-E and verify that the policy trained with grasps calculated in synthetic data performs well in the real world.

Compared to Dex-Net [3] that performs force-closure metric based on 3D object models, our ODG-Generation can generate positive grasps for objects with sharp edges, which is shown

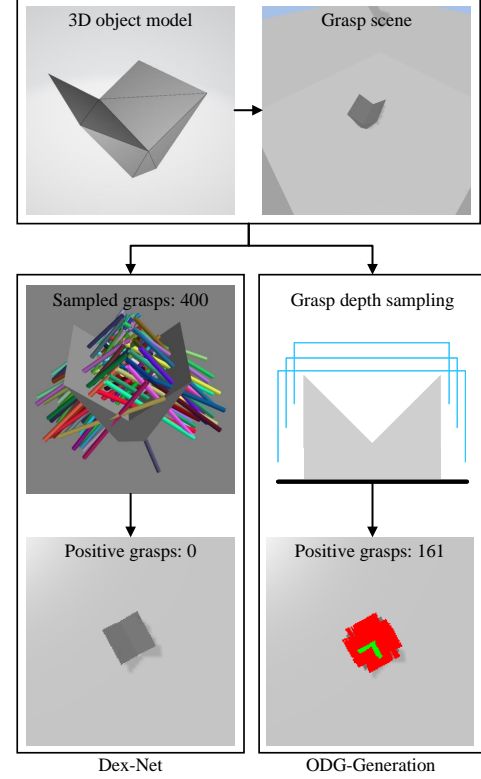


Fig. 6. The positive grasps for objects with sharp edges of Dex-Net and ODG-Generation. Dex-Net is useless in such scene, and our ODG-Generation utilizes orthographic depth images to transform sharp edges of objects into flat surfaces, resulting in positive grasps.

in Fig. 6. Dex-Net cannot compute valid friction cones based on points on sharp edges to generate training grasps for such objects, which makes the distribution of training and testing policies different. In contrast, ODG-Generation utilizes orthographic depth images to transform sharp edges of objects into flat surfaces, resulting in positive grasps.

E. Evaluation

We design a bin picking benchmark for testing where 320 cluttered scenes are constructed using 77 seen objects and 77 novel objects. Seen objects refer to the objects used to construct the PLGP-Dataset. Both sets of objects are from model datasets including: 20 from ShapeNet [35], 8 from the YCB [36], and 49 from EGAD [37]. All objects are of different sizes, materials and shapes, and include food, utensils, tools, toys and other common life items. We further divide our test scenes into 4 categories according to the number of objects $m = \{5, 15\}$ and whether objects have been seen or novel.

To evaluate the performance, previous methods rely on the available information to calculate the grasp stability. The rectangle metric [13] considers a grasp as correct if the rotation error is less than 30° and the rectangle IOU is larger than 0.25, which do not take into account the impact of collisions or skidding. Fang *et al.* [6] believe that the correct grasp fits force-closure metric and collision detection. However, slight collisions sometimes do not cause the grasp to fail.

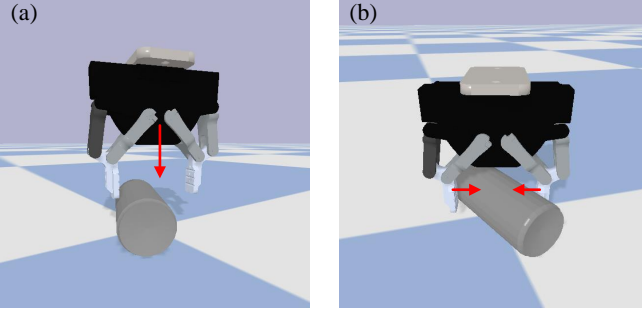


Fig. 7. (a) The grasp pose that causes the collision. (b) The grasp pose that does not achieve force-closure. As the gripper moves in the direction of the red arrow, the objects will be squeezed to a position suitable for grasping.

(a)		
successful grasps	1	6
total grasps	1	7
SR	1/1=100%	6/7=85.71%
PC	1/15=6.67%	6/15=40%

(b)		
rank=1	rank=30	rank=50
successful grasps	1	25
total grasps	1	30
AP	1/1=100%	25/30=83.33%

Fig. 8. The processes for calculating (a) Success Rate (SR), Percent Cleared (PC) and (b) Average Precision (AP). The scenes are initialized with 15 objects loaded. SR is the percentage of successful grasps out of total grasps. PC is the ratio of the successful grasps number to the objects number in the scene. AP is the percentage of successful grasps out of the top-50 grasps.

The objects in Fig. 7 will be squeezed by the gripper to a position suitable for grasping.

In this work, we adopt intuitive simulation grasp to evaluate the grasp accuracy. For each predicted grasp pose and friction coefficient, a simulated gripper is driven to the grasp pose to close and then lift, the prediction is correct if the object is lifted to the specified location. For cluttered scene, grasp pose prediction algorithms are expected to predict multiple grasps. We compare performance on this benchmark with the following metrics:

- **Success Rate (SR):** Objects in the scenes are grasped one by one with the first-ranked grasp until either (a) no objects remain or (b) the robot has 5 consecutive failed grasps. Success Rate measures the percentage of grasp attempts that lift an object.
- **Percent Cleared (PC):** The fraction of objects that are lifted when the aforementioned grasp ends [5].
- **Average Precision (AP):** The average precision of top-50

ranked grasps after NMS processing. The scene is reset to its initial state after each grasp process.

We report all metrics as the average of the results at different μ ranging from 0.2 to 1.0, with $\Delta\mu = 0.2$ as interval. The simulation grasp processes for calculating SR, PC and AP are shown in Fig. 8.

Our benchmark renders RGB-D images and point clouds of the test scene in real-time after loading the object model according to the published poses. Other methods can read the required visual information to generate the grasp pose, and obtain the grasp results of the simulated gripper in real time for comparison.

IV. NETWORK

A. Network Architecture

Fully convolutional network (FCN) [41] is selected as the basic structure of our network since the grasp label is pixel-level. FCN is widely used for semantic segmentation of images [42–45]. Our previous work [8] prove that FCN is effective for predicting dense grasp poses. We construct a pixel-level grasp detection network based on our previous network, AFFGA-Net [8]. AFFGA-Net first extracts features of different receptive fields and scales through the ResNet-101 network and the hybrid atrous spatial pyramid module, and then fuses the features according to different degrees of attention through an adaptive decoder, and finally outputs the grasping parameters through three task heads. Efficient feature extraction and decoding capabilities enable AFFGA-Net to perform best on the Cornell dataset [13].

We retain the encoder-decoder structure of AFFGA-Net as backbone and only modify the final task head to output grasp set $\tilde{G} = [Q_p, Q_\theta, W_g]$. \tilde{G} denotes the set of all grasps and corresponding qualities in the image space of size $H \times W$. We use Q_p to denote an output map of size $H \times W$ that represents the quality of a grasp executed at each point p . Q_θ is an output map of size $K \times H \times W$, which is used to represent the quality of the grasp run at point p with angle category k , from which we calculate the grasp angle by $\theta = \frac{\pi}{K}k$. The values of Q_p and Q_θ are scalars in the range $[0, 1]$ where a value closer to 1 indicates higher quality. W_g is an output map of size $K \times H \times W$, which is used to represent the required gripper width w to execute a grasp at point p with angle $\theta = \frac{\pi}{K}k$. The value of W_g are in range of $[0, 1]$, and gripper width w is obtained by multiplying W_g by L_4 . Given the highest quality point p , highest quality angle θ and gripper width w , grasp depth d is calculated from the depth image so that the gripper does not collide with the scene, and d does not exceed L_3 . The network structure is shown in Fig. 9. The input to networks is an optional single RGB image, a depth image or a concatenate RGB-D image.

To test the effect of different backbones on the experimental results, we replace the backbone module with the previous grasp detection networks GGCNN2 [46][47], GRCNN [48] and semantic segmentation networks UNet [49], SegNet [50], DANet [51], DeepLabv3+ [52] and STDC [53]. The results are reported in Sec.V-D.

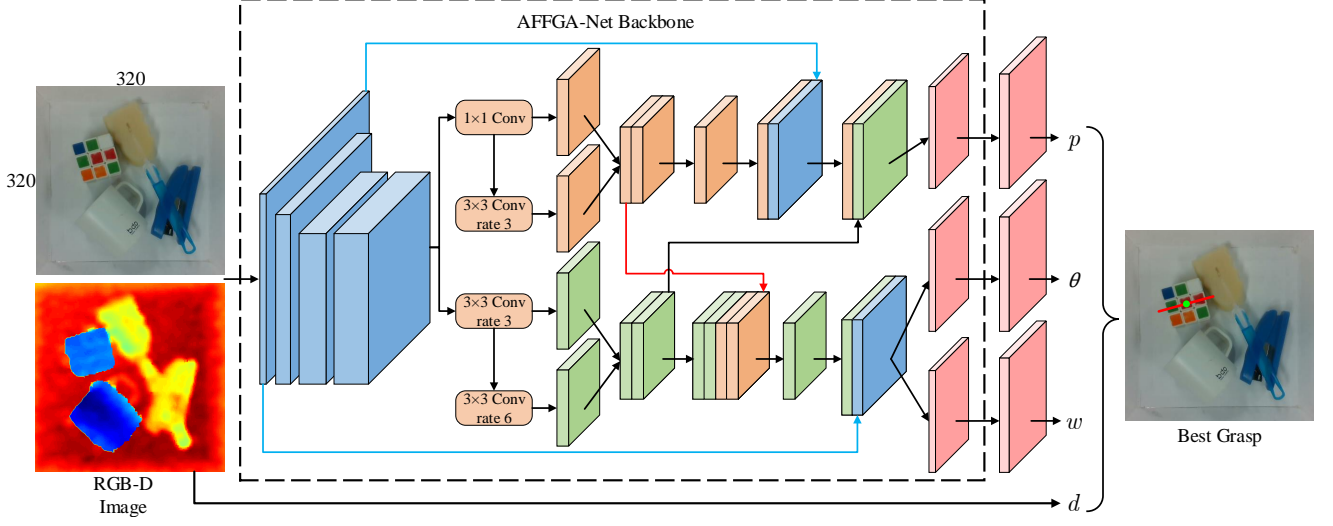


Fig. 9. Overview of our network. For a RGB-D image with $H \times W$ points as input, the network output the grasp quality, grasp angle quality and grasp width for every point. Given the highest quality point p , highest quality angle θ and gripper width w , grasp depth d is calculated from the depth image so that the gripper does not collide with the scene.

B. Augmentation and Normalization

We take all annotated grasp poses as positive samples and other grasp poses in the grasp parameter space as negative samples, and assume that all negative samples are unstable grasp poses. In PLGP-Dataset, the ratio of positive and negative samples is 1:1439. Significant imbalances in the number of samples degrade performance. In addition to using the focal loss function [54] to reduce the difference in loss of different samples, we also perform data augmentation on positive samples. Specifically, we copy the labeled grasp to other locations in its eight-neighborhood. The ratio is 1:317 after data augmentation. In Sec. V-A, we verify that data augmentation can effectively improve performance.

In order to facilitate the training of our network, we normalize the input depth image and learning target as follows.

Grasp quality. We treat grasp quality of each point as a scalar in the range $[0, 1]$. We set the already labeled grasp points a value of 1, and set the enhanced points a value of 0.9. All other points are 0.

Grasp angle. Each grasp angle θ is labeled in the range $[0, \pi]$. We convert the angle θ into category $k = \lfloor \frac{\theta}{\pi} K \rfloor$, where $K = 18$. We treat the quality of the grasps run at point p with angle category k as a scalar in the range $[0, 1]$. The already labeled grasp angles are set to 1, and the enhanced grasp angles are set to 0.9. All other angles are 0.

Gripper width. We scale the values of w by $\frac{1}{L_4}$ to put it in the range $[0, 1]$.

Input images. To augment the dataset, we perform data augmentation on images. We take a centre crop of 320×320 pixels with random translation up to 30 pixels horizontally and vertically. This image patch is then randomly rotated up to 30 degrees in both clock-direction and anticlock-direction. Then the image is randomly flipped horizontally. Finally, we subtract the mean of each image, centering its value around 0 to provide invariance.

C. Loss Function

Since the values of the network output map are all in the range of $[0, 1]$, the sigmoid function is used to activate the output value. GGCNN2 [46][47] uses the mean square error function to calculate the loss. However, the update rate is very slow when the prediction is close to the ground truth. We use the binary focal loss function to calculate the loss to avoid gradient reduction and reduce the loss difference between positive and negative samples. The loss function is defined as:

$$L(P, P^*, H, W, K) = -\frac{1}{N} \sum_{i=0}^H \sum_{j=0}^W \sum_{k=0}^K ((P_{ijk}^* \cdot \log(P_{ijk})) + (1 - P_{ijk}^*) \cdot \log(1 - P_{ijk}) \cdot |P_{ijk} - P_{ijk}^*|^\gamma \cdot \alpha),$$

where $\alpha = \mathbf{1}(P_{ijk}^* > 0) \cdot \alpha + (1 - \mathbf{1}(P_{ijk}^* > 0)) \cdot (1 - \alpha)$

(15)

where P is the output map of size $K \times H \times W$, P^* is training target, γ is set to 2 as recommended by [54]. Our network has the highest success rate in test scenarios when α is set to 0.95.

During training, the whole network is updated by minimizing the follow objective function:

$$L_{total} = \beta_1 \cdot L(Q_p, Q_p^*, H, W, 1) + \beta_2 \cdot L(Q_\theta, Q_\theta^*, H, W, K) + \beta_3 \cdot L(W_g, W_g^*, H, W, K)$$
(16)

where β_1 , β_2 and β_3 are weight coefficients of the loss. In our study, we experimentally set $\beta_1 = 10$, $\beta_2 = 10$ and $\beta_3 = 20$.

V. EXPERIMENTS

In this section, we experimentally demonstrate the advantages of our method under different experiments and comparisons. From extensive experiments, we aim to investigate:

- Do binary focal loss function and data augmentation improve neural network performance?

- Is network performance sensitive to label sparsity?
- Does our on-policy method perform better than previous off-policy methods using the same network structure and dataset scale?
- Does our network perform better than previous networks trained on the same dataset?
- How well does the grasp method that is learn entirely on simulated datasets perform in real scenarios?

In experiments, all neural networks are implemented with PyTorch and trained with Adam optimizer [55] on a PC running Ubuntu 16.04 with a 3.5GHz Intel Core i9-9900 CPU and NVIDIA TITAN-XP graphics card. The initial learning rate is set to 0.001. Networks are trained end-to-end for 100 epochs and learning-rate decays by a factor of 0.1 at 70 epochs.

A. Augmentation and Loss

In order to verify the effectiveness of binary focal loss function and data augmentation, we conduct ablation studies on the test scenes containing 15 novel objects, and the network input is a depth image. We follow the steps below to improve the AFFGA-Net and test its performance. (1) Modify the final task head to output grasp set \tilde{G} . (2) Perform data augmentation on labeled grasps. (3) Use the binary focal loss function instead of the binary cross-entropy function to calculate the loss. (4) Combination of (2) and (3).

All networks are trained on the PLGP-Dataset and results are reported in Table II. Baseline achieves only 24.41%, 18.02% and 39.81% on the SR, PC and AP, respectively. Data augmentation improves accuracies by 31.46%, 60.13% and 44.33%, and binary focal loss function improves accuracies by 38.90%, 66.73% and 43.04% compared to the baseline, respectively. The great improvement is due to data augmentation and binary focal loss significantly alleviating the imbalance of positive and negative samples. Combining data augmentation and binary focal loss function gives the highest accuracies.

B. Experiments of Sparse Label

To investigate how sensitive network performance is to sparse labels, we test the performance of AFFGA-Net under different pixel strides and grasp angle bins. Using different pixel strides s , we only compute the loss at coordinates that are integer multiples of s . The loss function is defined as:

$$L'_{ij} = \begin{cases} L_{ij}, & \text{if } i = s \cdot n \text{ and } j = s \cdot m \\ 0, & \text{otherwise} \end{cases} \quad (17)$$

where $n \in \mathbb{N}$ and $m \in \mathbb{N}$, L_{ij} is the original binary focal loss function. Using different grasp angle bins b , we convert the grasp angle category k in the dataset to a new category k' by $\frac{k \cdot b}{K}$.

All networks are trained on the PLGP-Dataset and tested on the test scenes containing 15 novel objects, and the network input is a depth image. Data augmentation for grasps is not used. Results are reported in Fig. 10. As the pixel stride increases, the AP value gradually decreases, and the difference exceeds 10% when stride is equal to 16, while SR and PC remain stable. The results show that as the training grasps

TABLE II
ABLATION STUDIES.

Baseline	Augmentation	BFL	SR (%)	PC (%)	AP (%)
✓			24.41	18.02	39.81
✓	✓		55.87	78.15	84.14
✓		✓	63.31	84.75	82.85
✓	✓	✓	65.61	84.79	87.37

* **BFL**: Binary focal loss function.

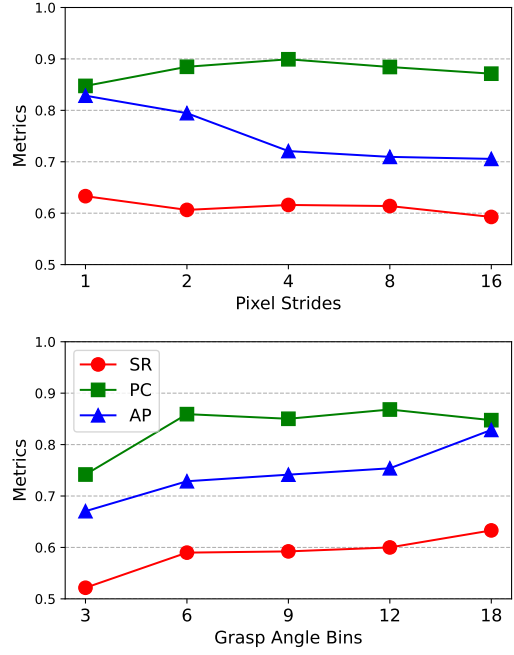


Fig. 10. Sensitivity of AFFGA-Net performance to sparse labels, in particular varying pixel strides and grasp angle bins.

decrease, the deviation of the network's fit to extreme points increases gradually. As the grasp angle bin decreases, both SR and AP gradually decrease, and PC decreases rapidly when the angle bin is less than 6. The results show that grasping is prone to failure when the error between the predicted grasp angle and the label exceeds 30°, which is coincident with the grasping rectangle metric [13].

C. On-policy VS Off-policy

In this experiment, we assume that the masks of objects in the scene are known, and set the grasp distribution for policy verification to all grasps where the grasp points lie within the object regions. Our method ODG-Generation is the on-policy baseline: it traverses all grasps in the object regions, and takes the grasps that satisfy the checks in Sec. III-D as positive, and other grasps as negative. On the contrary, we reimplement the following off-policy methods to generate labels separately and compare the performance of AFFGA-Net after training on different labels:

- **Dex-Net-400**: Sample 400 antipodal grasps on the surface of 3D object models and then project into image space [3].

TABLE III
EVALUATION OF AFFGA-NET BASED ON DIFFERENT GRASP LABEL GENERATION METHODS.

Method	Seen (%)						Novel (%)					
	5 objects		15 objects		5 objects		15 objects		5 objects		15 objects	
	SR	PC	AP									
Dex-Net-400 [3]	68.64	95.85	77.52	59.99	80.78	68.31	68.75	94.45	83.11	58.89	80.07	72.10
Dex-Net-1000 [3]	69.12	96.45	67.39	61.07	81.80	60.69	70.58	94.25	81.20	60.78	80.23	69.44
Manual [8]	71.89	96.15	82.78	61.71	82.42	66.43	68.44	95.85	74.13	59.66	81.82	72.72
ODG-Generation	79.77	98.10	85.24	71.33	89.82	74.01	71.87	97.85	85.29	63.73	89.48	75.00

- **Dex-Net-1000:** Sample 1000 antipodal grasps on the surface of 3D object models and then project into image space [3].
- **Manual:** Manual labeling [8].

To ensure that the experimental results are not disturbed by differences in training images, we construct a dataset using 77 seen object models from the PLGP-Dataset test set where 770 simulated train scenes are constructed. For each train scene, we adopt the ODG-Generation, Dex-Net-400, Dex-Net-1000, and Manual methods to generate grasp labels respectively. In Dex-Net, the grasp width is set to 0.08m which adapts to the size of all objects. During training, only the loss for the positive and negative grasps is computed.

The positive grasp labels of different methods are shown in Fig. 11, and the labels count and computation time of different methods are shown in Table IV. Grasp points of both ODG-Generation and Dex-Net are on the center axis of the object. The manual labels only contain the positive grasps that are easy to judge, and the points near the central axis of the object are marked as grasp points, which is similar to the role of data augmentation in Sec. IV-B.

We use different labels and the same images to form training sets respectively, and train AFFGA-Net to avoid the interference of different network structures on the experimental results. The network input is a depth image. To compare the impact of the original labels generated by different methods on the network performance, data augmentation was not used. All networks are tested on the test set of PLGP-Dataset, and the results are shown in Table III.

Both Dex-Net and ODG-Generation employ force closure to generate labels, but the distribution difference between training and testing of Dex-Net (i.e., off-policy) degrades performance. Compared with Dex-Net-1000, Dex-Net-400 with fewer training samples reduces the SR and PC metrics of the network, but improves the AP metrics. This may be because fewer training samples make the top-50 grasps clustered in easy-to-grasp locations. Manual label compensates for the negative effect of scarce positive grasps with the positive effect of data augmentation, thus achieving performance close to Dex-Net-1000. Compared with other methods, our ODG-Generation achieves the highest performance under all metrics.

D. Experiments of networks

We first test the different backbone networks in the benchmark. Then we test different representative methods on our

TABLE IV
GRASP LABEL STATISTICS FOR DIFFERENT METHODS.

Method	Positive	Negative	Total	Time per image	Time per object
Dex-Net-400 [3]	214.9K	44.2K	259.1K	7s	300s
Dex-Net-1000 [3]	537.2K	110.6K	647.7K	17s	880s
Manual [8]	2,294.1K	243.3M	245.6M	100s	10s
ODG-Generation	1,148.0K	244.4M	245.6M	400s	40s

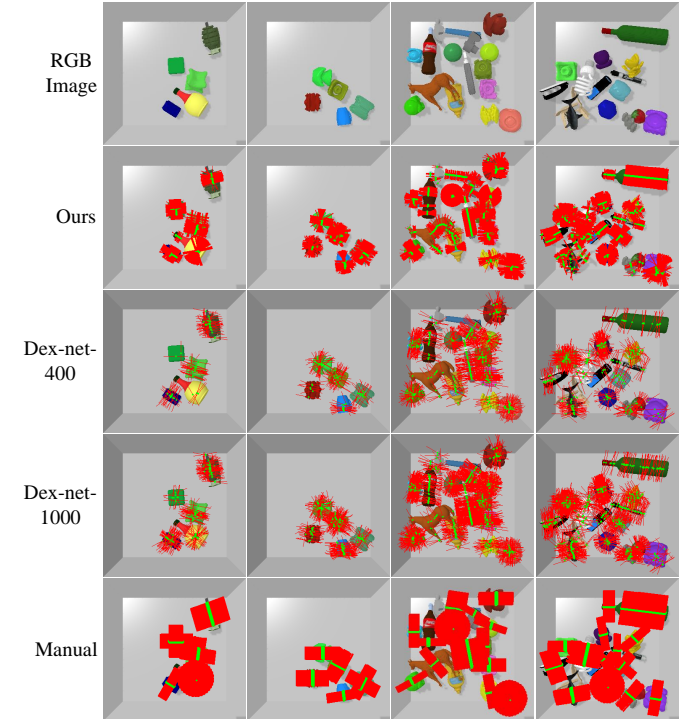


Fig. 11. RGB images and corresponding positive grasp labels generated by our ODG-Generation, Dex-Net, and Manual annotations.

benchmark and compare them with our method.

For depth image based method, we adopt GQCNN [3] and FC-GQCNN [9]. For point cloud based method, we adopt GraspNet [6]. GQCNN first samples multiple candidate grasp poses based on the depth image, and then input the image patch centered on the grasp point together with the point cloud into the grasp quality classification network to

TABLE V
EVALUATION FOR NETWORKS WITH DIFFERENT BACKBONE ON BENCHMARK.

Backbone	Input	Seen (%)						Novel (%)						Params (M)	GFLOPs
		5 objects			15 objects			5 objects			15 objects				
		SR	PC	AP	SR	PC	AP	SR	PC	AP	SR	PC	AP		
GGCNN2	Depth	70.49	94.47	77.87	59.96	72.47	66.99	68.40	90.06	86.15	62.59	81.63	75.18	0.079	1.36
	RGB	59.88	82.54	77.97	47.80	47.46	57.65	27.46	43.02	28.43	27.00	20.48	7.49	0.083	1.56
	RGB-D	65.34	89.80	75.68	50.85	57.54	62.86	29.26	52.80	30.33	32.16	30.20	6.47	0.085	1.66
GRCNN	Depth	73.44	95.74	82.92	60.87	77.18	72.05	75.49	93.13	89.47	68.05	84.63	82.70	1.90	13.38
	RGB	60.17	83.67	72.76	48.84	51.32	55.46	27.85	46.38	28.25	30.68	25.66	6.36	1.90	13.64
	RGB-D	64.43	88.01	77.61	51.27	58.76	59.25	30.47	55.71	29.84	33.97	35.30	7.23	1.91	13.77
UNet	Depth	73.74	93.92	83.89	61.74	72.58	76.98	76.95	93.43	88.39	67.20	84.20	79.90	34.53	50.18
	RGB	67.65	89.82	74.96	50.44	51.25	55.14	63.14	82.33	81.74	55.51	57.98	66.92	34.53	50.24
	RGB-D	63.75	86.17	75.67	52.20	55.47	60.90	61.91	88.19	82.98	56.48	65.35	68.30	34.53	50.27
SegNet	Depth	73.94	95.03	84.89	62.18	76.25	73.13	76.34	93.33	89.05	67.19	84.66	79.12	29.54	35.41
	RGB	66.66	91.17	76.74	51.42	56.04	64.42	65.21	85.55	83.05	57.22	64.34	67.41	29.54	35.46
	RGB-D	64.58	89.33	80.40	54.01	64.52	66.46	62.34	88.24	84.57	59.08	73.91	71.52	29.54	35.49
DeepLabv3+	Depth	55.30	79.29	73.23	50.52	55.15	71.12	66.17	87.65	83.54	62.21	77.75	78.14	62.02	83.45
	RGB	54.26	77.47	66.69	45.62	43.95	58.94	59.96	83.27	79.75	55.18	60.44	71.41	62.02	83.53
	RGB-D	56.20	80.27	69.20	47.02	48.64	64.63	58.81	84.93	82.17	52.77	60.88	66.55	62.03	83.57
STDC	Depth	74.49	96.17	82.43	62.10	73.74	71.60	75.02	93.18	90.68	68.00	85.49	82.66	47.58	39.25
	RGB	67.18	92.03	80.41	50.92	53.51	60.80	65.66	83.37	82.02	57.13	63.42	71.87	47.58	39.26
	RGB-D	61.62	82.32	77.08	52.97	59.83	61.96	63.71	86.68	86.10	57.28	69.15	73.10	47.58	39.27
DANet	Depth	81.31	96.22	87.79	69.43	86.55	76.59	80.11	94.28	89.59	69.25	85.64	78.14	26.18	25.33
	RGB	69.87	92.84	82.86	55.78	64.15	66.14	66.74	87.67	83.16	60.67	69.16	68.64	26.19	25.36
	RGB-D	79.29	96.60	87.97	68.37	79.83	76.73	74.42	91.40	89.97	67.24	79.49	77.06	26.19	25.37
AFFGA-Net (Ours)	Depth	83.14	96.39	84.67	75.30	85.84	75.25	80.41	92.02	91.13	65.61	84.79	87.37	67.59	29.58
	RGB	74.40	86.71	77.66	71.02	75.65	74.65	82.92	94.07	90.68	63.24	67.42	75.71	67.60	29.67
	RGB-D	85.59	96.20	89.47	78.81	85.78	78.33	84.48	96.80	94.07	70.86	84.87	85.49	67.60	29.70

obtain the quality of each candidate grasp pose. FC-GQCNN outputs multiple 4-DOF grasp poses and qualities on depth images end-to-end. GraspNet takes point cloud as input and predicts approaching direction, grasp pose and quality through three network modules connected in series. Since the output data formats are different, we adopt the public weights of GQCNN, FC-GQCNN and GraspNet which are trained on Dex-Net 4.0 [3], Dex-Net 2.0 [4] and GraspNet-1Billion [6] datasets, respectively. The GraspNet-1Billion is created using the grasping generation method of Dex-Net 2.0.

The experimental results of networks built on different backbones when inputting depth images, RGB images, and RGB-D images are shown in Table V.

Comparing the results of the same network with different input, the network with depth image as input has better performance than RGB image, because the depth image contains the shape information of the objects. The difference in accuracy is especially noticeable in lightweight networks, because it is difficult for lightweight networks to extract shape features related to grasping from color information. For example, the differences between SR, PC and AP of GGCNN2 with RGB images and depth images as input in scenes containing 5 novel objects are 40.94%, 47.04% and 57.72%, respectively, while the differences of UNet are 13.81%, 11.10% and 6.65%. In addition, the results of complex networks with RGB-D images and depth images as input is similar, while the accuracy of

lightweight networks with RGB-D images as input is lower, which is due to the inability of lightweight networks to fit complex sample distributions.

Compared with complex networks or lightweight networks with depth images as input, lightweight networks with RGB and RGB-D images as input have a larger accuracy gap between seen objects and novel objects, and the gap in AP is more obvious in the scene containing 15 objects. This indicates that lightweight networks with RGB image as input are more prone to overfitting, and the actual quality of predicted grasp pose drops drastically as the predicted quality decreases.

Comparing the results of the same network in scenes with different levels of complexity, all networks perform better in scenes containing 5 objects, because complex scenes have low fault tolerance for grasp poses, slight grasp point errors and collisions can cause objects to move and fail to grasp.

Besides, networks taking depth images as input are less affected by scene complexity than networks taking RGB images as input, because color information cannot reflect the positional relationship of stacked objects. For example, the differences between SR, PC and AP of STDC with depth images as input in scenes containing 15 and 5 seen objects are 7.02%, 7.69% and 8.02%, respectively, while the differences of STDC with RGB images as input are 8.53%, 19.95% and 10.15%.

Comparing the results of different networks under the same

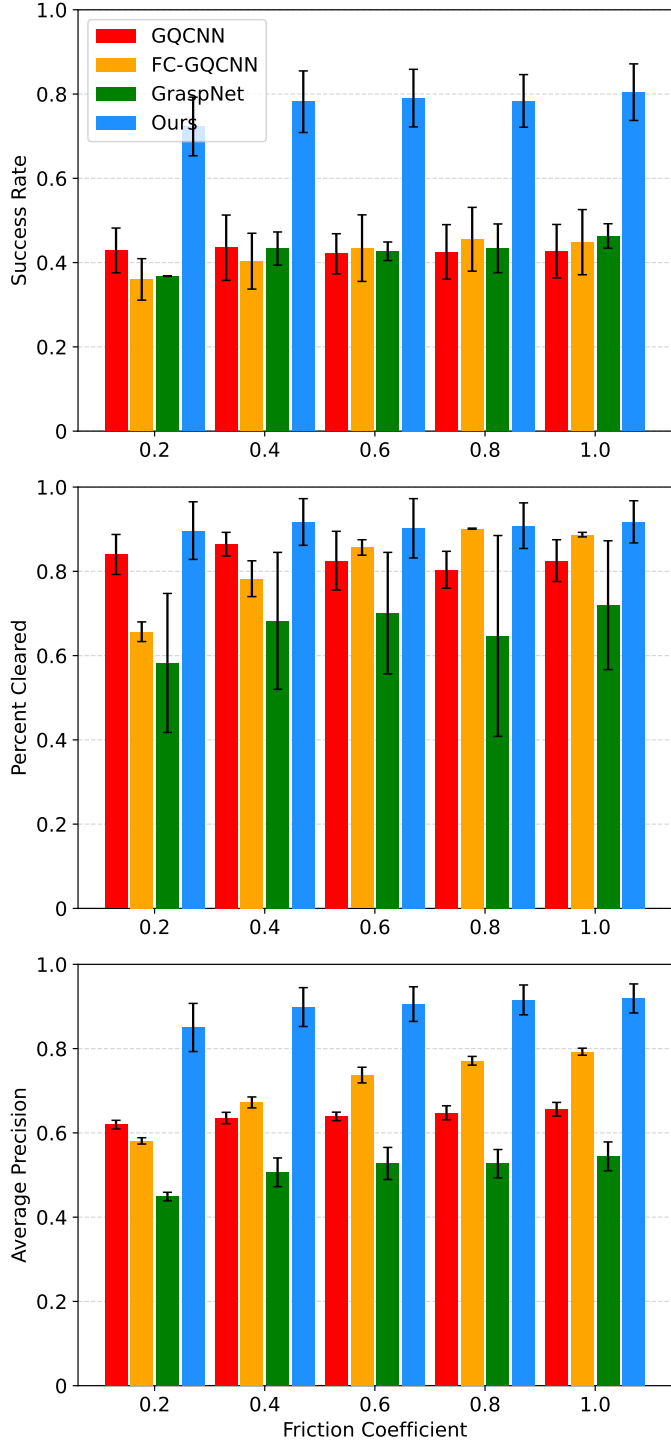


Fig. 12. The SR, PC and AP of different methods under different friction coefficients. The value and error of each bar are the mean and difference of the method's metrics in scenes with 5 and 15 objects, respectively.

input, our AFFGA-Net performs best. The reason contribute to this achievement is, the hybrid atrous spatial pyramid module extracts features of different receptive fields and scales, and the adaptive decoder provides the most relevant features for different prediction tasks. DeepLabv3+, which is popular in the semantic segmentation, is inferior to UNet in the grasp detection task. This is because DeepLabv3+ directly enlarges the feature map by upsampling to obtain the prediction map by 4 times, and cannot accurately recover the pixel-level grasping pose.

We separately test the performance of GQCNN, FC-GQCNN and GraspNet in benchmark scenes containing novel objects, and compare with our network. The SR, PC and AP of the methods under different friction coefficients are shown in Fig. 12, and the mean values of SR, PC and AP under different friction coefficients are shown in Table VI. The results show that our method outperforms other methods at all friction coefficients and metrics.

Compared with GQCNN, even the light-weight network GGCNN with depth images as input improves the SR, PC and AP metrics of scenes containing 5 unknown objects by 31.78%, 2.11% and 20.86%, respectively. Apart from the differences in dataset and network, an important reason for the better performance of our methods is that, the Dex-Net and GraspNet-1Billion datasets generate grasp labels based on 3D object models, which makes the data distribution of training and testing different, thereby reducing the generalization ability of GQCNN, FC-GQCNN and GraspNet. In addition, the candidate grasps randomly generated by GQCNN cannot be guaranteed to be globally optimal and cannot cover the grasp parameter space. This further shows that datasets with on-policy and pixel-level attributes can effectively improve grasp detection performance.

E. Real-world Grasping

To perform robotic grasping experiments, we use a Kinova Gen2 7DOF robot fitted with a robotiq 2f-140 gripper. Our camera is an Intel RealSense D435i RGB-D camera and is mounted to the wrist of the robot. We selected 40 objects of different shapes, sizes, and materials for testing. This set-up is shown in Fig. 13.

We conduct three sets of experiments to separately test the performance of AFFGA-Net in scenes containing $M = \{1, 5, 10\}$ objects. Objects are randomly ordered and numbered before the experiment began. In the initial state of each scene, we select M objects in number order and place them randomly in the tray. On each timestep, with the AFFGA-Net, we input a depth image and camera intrinsics, and output the grasp pose with highest predicted quality. The robot then approaches the target and closes the jaws (Fig. 14). Grasp success is defined by whether or not the grasp transport the target object to the receptacle. If there are no objects in the tray or the robot has 5 consecutive failures, the next scene will be tested. Each object is placed in the tray a total of 10 times.

Table VII shows the performance. We conduct a total of 2,428 grasping trials, and the total number of failed grasps is 28. Grasping success rate decreases as the test scenes contains

TABLE VI
EVALUATION FOR DIFFERENT METHODS ON BENCHMARK.

Method	Input	5 objects			15 objects		
		SR (%)	PC (%)	AP (%)	SR (%)	PC (%)	AP (%)
GQCNN [3]	Depth	36.62	87.95	65.29	48.88	78.42	62.62
FC-GQCNN [9]	Depth	35.08	83.45	69.92	48.98	79.92	72.24
GraspNet [6]	Point cloud	45.48	83.90	54.08	39.53	49.38	48.07
AFFGA-Net (Ours)	RGB-D	84.48	96.80	94.07	70.86	84.87	85.49



Experimental Setup



Test Objects

Fig. 13. Left: Set-up for robotic grasping experiments. For each experiment, M objects are randomly dropped on the tray, at which point the robot iteratively plans grasps from RGB-D image and attempts to lift and transport the objects to a receptacle. Right: A set of 40 test objects.

more objects, because stacked objects increase the error of the depth images and squeeze the positive grasping parameter space. However, the success rate in the scenes consisting of 10 objects still reaches 95.92%. Meanwhile, the percent cleared are 100% in all experiments. There are three main types of failed grasping: (1) Adjacent objects are grasped at the same time, and drop during lift; (2) Large cylindrical objects cannot be grasped when placed vertically; (3) Objects with sloping edges cannot be grasped. The first kind of failure is due to the inability of the network to distinguish two objects that are in close proximity. The second kind of failure is due to fewer training scenes with upright cylindrical objects in the PLGP-Dataset. The third kind of failure is due to the low friction coefficient threshold (i.e. 0.2) for filtering out candidate grasp poses in the ODG-Generation method, resulting in fewer grasp pose labels on objects with sloping edges. The experimental procedure is shown in the supplemental video.

VI. CONCLUSION

In this paper, we propose an on-policy grasp detection method. First, the ODG-Generation method is introduced to compute pixel-level grasp labels based on orthographic depth images, which trains and tests the grasping network on the same distribution, and improves the generalization ability of

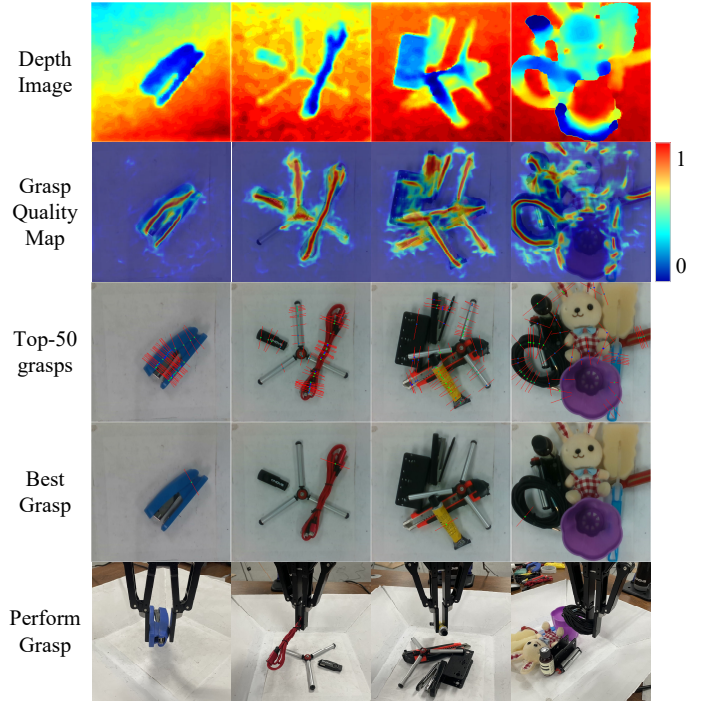


Fig. 14. Experiments for real-world robotic grasping.

TABLE VII
ROBOTIC GRASP RESULTS.

Objects	SR (%)	PC (%)	Attempts	Failures
1	99.01	100	404	4
5	98.28	100	407	7
10	95.92	100	417	17

the network. Then, the first on-policy pixel-level grasp detection dataset PLGP-Dataset is constructed and released based on ODG-Generation method. It consists of images taken by the simulated sensor, with rich and dense annotations. At last, we construct a series of grasp detection networks equipped with a novel data augmentation mode. Extensive experiments demonstrate the superiority of our method in both bin-picking benchmark and real grasping. Our future work is to expand the dataset and drive the robot to push objects autonomously to improve grasping success rate.

ACKNOWLEDGMENT

This work is supported in part by National Natural Science Foundation of China (62176138, 62176136), National Key R&D Program of China (NO.2018YFB1305300), Shandong Provincial Key Research and Development Program (Major Scientific and Technological Innovation Project) (NO.2019JZZY010130, 2020CXGC010207).

REFERENCES

- [1] N. D. Kahanowich and A. Sintov, “Robust classification of grasped objects in intuitive human-robot collaboration using a wearable force-myography device,” *IEEE Robotics and Automation Letters*, vol. 6, no. 2, pp. 1192–1199, 2021.
- [2] F. Y. Wu and H. H. Asada, “Implicit and intuitive grasp posture control for wearable robotic fingers: a data-driven method using partial least squares,” *IEEE Transactions on Robotics*, vol. 32, no. 1, pp. 176–186, 2016.
- [3] J. Mahler, M. Matl, V. Satish, M. Danielczuk, B. DeRose, S. McKinley, and K. Goldberg, “Learning ambidextrous robot grasping policies,” *Science Robotics*, vol. 4, no. 26, 2019.
- [4] J. Mahler, J. Liang, S. Niyaz, M. Laskey, R. Doan, X. Liu, J. A. Ojea, and K. Goldberg, “Dex-net 2.0: Deep learning to plan robust grasps with synthetic point clouds and analytic grasp metrics,” in *Robotics: Science and Systems*, 2017.
- [5] M. Jeffrey and G. Ken, “Learning deep policies for robot bin picking by simulating robust grasping sequences,” in *Conference on robot learning*, pp. 515–524, 2017.
- [6] H.-S. Fang, C. Wang, M. Gou, and C. Lu, “Graspnet-1billion: A large-scale benchmark for general object grasping,” in *Proceedings of the IEEE/CVF conference on computer vision and pattern recognition*, pp. 11444–11453, 2020.
- [7] Z. Binglei, Z. Hanbo, L. Xuguang, W. Haoyu, T. Zhiqiang, and Z. Nanning, “Regnet: Region-based grasp network for end-to-end grasp detection in point clouds,” in *2021 IEEE International Conference on Robotics and Automation (ICRA)*, pp. 13474–13480, 2021.
- [8] D. Wang, C. Liu, F. Chang, N. Li, and G. Li, “High-performance pixel-level grasp detection based on adaptive grasping and grasp-aware network,” *IEEE Transactions on Industrial Electronics*, 2021.
- [9] V. Satish, J. Mahler, and K. Goldberg, “On-policy dataset synthesis for learning robot grasping policies using fully convolutional deep networks,” *IEEE Robotics and Automation Letters*, vol. 4, no. 2, pp. 1357–1364, 2019.
- [10] A. Zeng, S. Song, S. Welker, J. Lee, A. Rodriguez, and T. Funkhouser, “Learning synergies between pushing and grasping with self-supervised deep reinforcement learning,” in *2018 IEEE/RSJ International Conference on Intelligent Robots and Systems (IROS)*, pp. 4238–4245, 2018.
- [11] J. Schulman, F. Wolski, P. Dhariwal, A. Radford, and O. Klimov, “Proximal policy optimization algorithms,” *arXiv preprint arXiv:1707.06347*, 2017.
- [12] E. Coumans and Y. Bai, “Pybullet, a python module for physics simulation for games, robotics and machine learning,” <http://pybullet.org>, 2016–2021.
- [13] Y. Jiang, S. Moseson, and A. Saxena, “Efficient grasping from rgbd images: Learning using a new rectangle representation,” in *2011 IEEE International conference on robotics and automation*, pp. 3304–3311, 2011.
- [14] L. Pinto and A. Gupta, “Supersizing self-supervision: Learning to grasp from 50k tries and 700 robot hours,” in *2016 IEEE international conference on robotics and automation (ICRA)*, pp. 3406–3413, 2016.
- [15] S. Levine, P. Pastor, A. Krizhevsky, J. Ibarz, and D. Quillen, “Learning hand-eye coordination for robotic grasping with deep learning and large-scale data collection,” *The International Journal of Robotics Research*, vol. 37, no. 4-5, pp. 421–436, 2018.
- [16] A. Depierre, E. Dellandréa, and L. Chen, “Jacquard: A large scale dataset for robotic grasp detection,” in *2018 IEEE/RSJ International Conference on Intelligent Robots and Systems (IROS)*, pp. 3511–3516, 2018.
- [17] H. Zhang, X. Lan, S. Bai, X. Zhou, Z. Tian, and N. Zheng, “Roi-based robotic grasp detection for object overlapping scenes,” in *2019 IEEE/RSJ International Conference on Intelligent Robots and Systems (IROS)*, pp. 4768–4775, 2019.
- [18] F.-J. Chu, R. Xu, and P. A. Vela, “Real-world multiobject, multigrasp detection,” *IEEE Robotics and Automation Letters*, vol. 3, no. 4, pp. 3355–3362, 2018.
- [19] X. Yan, J. Hsu, M. Khansari, Y. Bai, A. Pathak, A. Gupta, J. Davidson, and H. Lee, “Learning 6-dof grasping interaction via deep geometry-aware 3d representations,” in *2018 IEEE International Conference on Robotics and Automation (ICRA)*, pp. 3766–3773, 2018.
- [20] J. Bohg, A. Morales, T. Asfour, and D. Kragic, “Data-driven grasp synthesis-a survey,” *IEEE Transactions on Robotics*, vol. 30, no. 2, pp. 289–309, 2013.
- [21] Y. Inagaki, R. Araki, T. Yamashita, and H. Fujiyoshi, “Detecting layered structures of partially occluded objects for bin picking,” in *2019 IEEE/RSJ International Conference on Intelligent Robots and Systems (IROS)*, pp. 5786–5791, 2019.
- [22] B. Wu, I. Akinola, A. Gupta, F. Xu, J. Varley, D. Watkins-Valls, and P. K. Allen, “Generative attention learning: a “general” framework for high-performance multi-fingered grasping in clutter,” *Auton. Robots*, vol. 44, no. 6, pp. 971–990, 2020.
- [23] S. R. Lakani, A. J. Rodríguez-Sánchez, and J. H. Piater, “Towards affordance detection for robot manipulation using affordance for parts and parts for affordance,” *Auton. Robots*, vol. 43, no. 5, pp. 1155–1172, 2019.
- [24] V.-D. Nguyen, “Constructing force-closure grasps,” *The International Journal of Robotics Research*, vol. 7, no. 3, pp. 3–16, 1988.
- [25] Q. Yu, W. Shang, Z. Zhao, S. Cong, and Z. Li, “Robotic grasping of unknown objects using novel multilevel

convolutional neural networks: From parallel gripper to dexterous hand,” *IEEE Transactions on Automation Science and Engineering*, 2020.

[26] I. Akinola, A. Angelova, Y. Lu, Y. Chebotar, D. Kalashnikov, J. Varley, J. Ibarz, and M. S. Ryoo, “Visionary: Vision architecture discovery for robot learning,” pp. 10 779–10 785, 2021.

[27] S. Ainetter and F. Fraundorfer, “End-to-end trainable deep neural network for robotic grasp detection and semantic segmentation from rgb,” in *2021 IEEE International Conference on Robotics and Automation (ICRA)*, pp. 13 452–13 458, 2021.

[28] F.-J. Chu, R. Xu, and P. A. Vela, “Real-world multi-object, multi-grasp detection,” *IEEE Robotics and Automation Letters*, vol. 3, no. 4, pp. 3355–3362, 2018.

[29] X. Zhu, D. Wang, O. Biza, G. Su, R. Walters, and R. Platt, “Sample efficient grasp learning using equivariant models,” in *Proceedings of Robotics: Science and Systems*, 2022.

[30] F. Alladkani, J. Akl, and B. Calli, “Ecnns: Ensemble learning methods for improving planar grasp quality estimation,” pp. 4769–4775, 2021.

[31] X. Zhu, L. Sun, Y. Fan, and M. Tomizuka, “6-dof contrastive grasp proposal network,” pp. 6371–6377, 2021.

[32] L. Berscheid, C. Friedrich, and T. Kröger, “Robot learning of 6 dof grasping using model-based adaptive primitives,” pp. 4474–4480, 2021.

[33] K. S. Andreas ten Pas, Marcus Gualtieri and R. P. Jr, “Grasp pose detection in point clouds,” *Int. J. Robotics Res.*, vol. 36, no. 13-14, pp. 1455–1473, 2017.

[34] Y. Qin, R. Chen, H. Zhu, M. Song, J. Xu, and H. Su, “S4g: Amodal single-view single-shot $se(3)$ grasp detection in cluttered scenes,” in *Conference on robot learning*, pp. 53–65, 2020.

[35] A. X. Chang, T. Funkhouser, L. Guibas, P. Hanrahan, Q. Huang, Z. Li, S. Savarese, M. Savva, S. Song, H. Su *et al.*, “Shapenet: An information-rich 3d model repository,” *arXiv preprint arXiv:1512.03012*, 2015.

[36] B. Calli, A. Walsman, A. Singh, S. Srinivasa, P. Abbeel, and A. M. Dollar, “Benchmarking in manipulation research: Using the yale-cmu-berkeley object and model set,” *IEEE Robotics & Automation Magazine*, vol. 22, no. 3, pp. 36–52, 2015.

[37] D. Morrison, P. Corke, and J. Leitner, “Egad! an evolved grasping analysis dataset for diversity and reproducibility in robotic manipulation,” *IEEE Robotics and Automation Letters*, vol. 5, no. 3, pp. 4368–4375, 2020.

[38] E. Johns, S. Leutenegger, and A. J. Davison, “Deep learning a grasp function for grasping under gripper pose uncertainty,” in *2016 IEEE/RSJ International Conference on Intelligent Robots and Systems (IROS)*, pp. 4461–4468. IEEE, 2016.

[39] S. Zennaro, M. Munaro, S. Milani, P. Zanuttigh, A. Bernardi, S. Ghidoni, and E. Menegatti, “Performance evaluation of the 1st and 2nd generation kinect for multimedia applications,” in *2015 IEEE International Conference on Multimedia and Expo (ICME)*, pp. 1–6, 2015.

[40] G. Smith, E. Lee, K. Goldberg, K. Bohringer, and J. Craig, “Computing parallel-jaw grips,” in *Proceedings 1999 IEEE International Conference on Robotics and Automation (Cat. No. 99CH36288C)*, vol. 3, pp. 1897–1903, 1999.

[41] J. Long, E. Shelhamer, and T. Darrell, “Fully convolutional networks for semantic segmentation,” in *Proceedings of the IEEE conference on computer vision and pattern recognition*, pp. 3431–3440, 2015.

[42] T. Zhou, W. Wang, S. Liu, Y. Yang, and L. Van Gool, “Differentiable multi-granularity human representation learning for instance-aware human semantic parsing,” in *Proceedings of the IEEE/CVF Conference on Computer Vision and Pattern Recognition*, pp. 1622–1631, 2021.

[43] L. Zhu, D. Ji, S. Zhu, W. Gan, W. Wu, and J. Yan, “Learning statistical texture for semantic segmentation,” in *Proceedings of the IEEE/CVF Conference on Computer Vision and Pattern Recognition*, pp. 12 537–12 546, 2021.

[44] T. Takikawa, D. Acuna, V. Jampani, and S. Fidler, “Gated-scnn: Gated shape cnns for semantic segmentation,” in *Proceedings of the IEEE/CVF International Conference on Computer Vision*, pp. 5229–5238, 2019.

[45] Y. Yuan, J. Xie, X. Chen, and J. Wang, “Segfix: Model-agnostic boundary refinement for segmentation,” in *European Conference on Computer Vision*, pp. 489–506, 2020.

[46] D. Morrison, P. Corke, and J. Leitner, “Learning robust, real-time, reactive robotic grasping,” *The International Journal of Robotics Research*, vol. 39, no. 2-3, pp. 183–201, 2020.

[47] D. Morrison, P. Corke, and J. Leitner, “Closing the loop for robotic grasping: A real-time, generative grasp synthesis approach,” *arXiv preprint arXiv:1804.05172*, 2018.

[48] S. Kumra, S. Joshi, and F. Sahin, “Antipodal robotic grasping using generative residual convolutional neural network,” in *2020 IEEE/RSJ International Conference on Intelligent Robots and Systems (IROS)*, pp. 9626–9633, 2020.

[49] O. Ronneberger, P. Fischer, and T. Brox, “U-net: Convolutional networks for biomedical image segmentation,” in *International Conference on Medical image computing and computer-assisted intervention*, pp. 234–241, 2015.

[50] V. Badrinarayanan, A. Kendall, and R. Cipolla, “Segnet: A deep convolutional encoder-decoder architecture for image segmentation,” *IEEE transactions on pattern analysis and machine intelligence*, vol. 39, no. 12, pp. 2481–2495, 2017.

[51] J. Fu, J. Liu, H. Tian, Y. Li, Y. Bao, Z. Fang, and H. Lu, “Dual attention network for scene segmentation,” in *Proceedings of the IEEE/CVF Conference on Computer Vision and Pattern Recognition*, pp. 3146–3154, 2019.

[52] L.-C. Chen, Y. Zhu, G. Papandreou, F. Schroff, and H. Adam, “Encoder-decoder with atrous separable convolution for semantic image segmentation,” in *Proceedings of the European conference on computer vision (ECCV)*, pp. 801–818, 2018.

- [53] M. Fan, S. Lai, J. Huang, X. Wei, Z. Chai, J. Luo, and X. Wei, “Rethinking bisenet for real-time semantic segmentation,” in *Proceedings of the IEEE/CVF Conference on Computer Vision and Pattern Recognition*, pp. 9716–9725, 2021.
- [54] T.-Y. Lin, P. Goyal, R. Girshick, K. He, and P. Dollár, “Focal loss for dense object detection,” in *Proceedings of the IEEE international conference on computer vision*, pp. 2980–2988, 2017.
- [55] D. P. Kingma and J. Ba, “Adam: A method for stochastic optimization,” *arXiv preprint arXiv:1412.6980*, 2014.